EREM 82/2
Journal of Environmental Research, Engineering and Management
Vol. 82 / No. 2 / 2026
pp. 80–101
10.5755/j01.erem.82.2.43606

Hybrid PSO–L-BFGS-B Optimization of Small-Scale HAWTs for Low-Wind Tropical Sites: Blades Length and Hub Height Tuning with Multi-Site Indonesian Data

Received 2025/11 | Accepted after revisions 2026/03

https://doi.org/10.5755/j01.erem.82.2.43606

# Hybrid PSO–L-BFGS-B Optimization of Small-Scale HAWTs for Low-Wind Tropical Sites: Blades Length and Hub Height Tuning with Multi-Site Indonesian Data

**Reza Istoni[1,2]*, Aziah Khamis[1], Zulkifli Ibrahim[1]**

[1] Faculty of Electrical Technology Engineering, Universiti Teknikal Malaysia Melaka, Malaysia

[2] Darma Persada University, Indonesia

***Corresponding author:** reza.istoni@gmail.com

Wind energy, offers strong potential for tropical regions, yet low and variable wind speeds limit the efficiency of conventional turbines. Therefore, this study proposes a hybrid optimization technique integrating particle swarm optimization (PSO) with the Limited-memory Broyden-Fletcher-Goldfarb-Shanno (L-BFGS-B) algorithm to determine the optimal blade length and hub height of small-scale horizontal axis wind turbines (HAWTs). Multi-year wind datasets (2017–2020) from five Indonesian sites Jambi, South Sulawesi, NTB, NTT, and Maluku were statistically characterized using Weibull and Bi-Weibull distribution and incorporated into annual energy production (AEP) modelling. The hybrid PSO–L-BFGS-B method achieved 5–15% higher AEP than standard PSO, and 11–25% higher AEP compared to the baseline TSD-500 turbine, while also exhibiting smoother convergence and reduced interquartile variability across 30 independent runs. Sensitivity analysis showed that hub height exerts a stronger influence on AEP than blade length, reflecting the aerodynamic advantage of elevated rotors under low-wind tropical conditions. The results demonstrate that hybrid meta-heuristic optimization effectively tailors small-scale wind turbines for reliable and sustainable energy generation in tropical developing regions.

**Keywords:** small-scale horizontal-axis wind turbine (HAWT), low-wind tropical sites, PSO–L-BFGS-B optimization, annual energy production (AEP).

## Introduction

Wind energy has emerged as one of the fastest-growing renewable energy technologies worldwide, playing a central role in global efforts to reduce greenhouse gas emissions and mitigate climate change. However, the technological development and large-scale deployment of wind turbines have historically been driven by temperate regions characterized by relatively high and stable wind speeds (Maulidia, 2019; Scott, 2019; Sambodo et al., 2022). Consequently, most commercial wind turbine designs remain optimized for such conditions. When deployed in tropical regions, these designs often experience significant performance degradation due to fundamentally different wind characteristics (Abbas et al., 2025). In low-wind tropical environments, wind regimes are typically defined by lower mean velocities, higher intermittency, and pronounced seasonal variability, which collectively limit the effectiveness of conventional turbine configurations (Baker et al., 2023; Svorcan et al., 2025).

Indonesia exemplifies the challenges associated with wind energy deployment in low-wind tropical regions (Darmawan, 2025). Although the country possesses substantial theoretical wind resources, practical utilisation remains limited, and installed wind capacity accounts for only a small fraction of national renewable energy targets. A key barrier is the continued reliance on imported turbine technologies designed for higher wind classes. Such turbines are poorly matched to Indonesia's prevailing wind conditions, where average wind speeds typically range between 3 and 4 m/s (Adrian et al., 2023; Yudha and Tjahjono, 2019). This mismatch leads to low capacity factors, reduced economic viability, and underperformance in decentralised and rural electrification applications. These limitations highlight the need for wind turbine design strategies that are explicitly adapted to tropical low-wind conditions rather than directly transferred from high-wind environments.

For small-scale horizontal-axis wind turbine (HAWT), blade length and hub height are two design variable with a direct and practical influence on annual energy production (AEP) (Zhu et al., 2016). Increasing blade length enlarges the rotor swept area and enhances wind energy capture at low wind speeds, but it also introduces higher aerodynamic loads and structural constraints (Luo et al., 2025). Similarly, increasing hub height enables access to stronger and less turbulent wind layers; however, taller towers increase material requirements, construction complexity, and maintenance costs (Scott, 2019). These competing effects indicate that performance enhancement in low-wind tropical environments is not solely an aerodynamic problem, but rather a constrained optimization task that requires balancing energy yield with practical and structural considerations.

Small-scale HAWTs are commonly classified based on rotor diameter and rated power, which directly influence their aerodynamic behavior, structural requirements, and application scope. In general, small-scale HAWTs are characterized by rotor diameters below approximately 10 m and rated power capacities typically below 100 kW, making them suitable for decentralized and rural energy applications. Recent studies have shown that systematic aerodynamic optimization of small-scale HAWTs, particularly when combined with surrogate-based and response surface methods, can significantly enhance performance under low and variable wind conditions (Van et al., 2024).

As an alternative configuration, vertical-axis wind turbines (VAWTs), particularly Darrieus-type designs, have also been investigated for small-scale wind energy applications. VAWTs offer advantages such as omnidirectional wind acceptance and potentially simpler mechanical layouts; however, their aerodynamic efficiency and self-starting characteristics remain strongly dependent on blade design and flow control strategies (Subramanian et al., 2025). Recent investigations into passive aerodynamic modifications, including Kline–Fogleman trailing-edge designs, have demonstrated efficiency improvements for Darrieus VAWTs in small-scale applications. Nevertheless, for low-wind tropical environments, HAWTs generally remain more favorable in terms of energy yield and technological maturity (Budanko and Guzović, 2024). Accordingly, this study focuses on small-scale HAWTs as a practical and widely deployed technology for decentralized energy generation.

To address such constrained and nonlinear design problems, a wide range of optimization techniques has been applied in wind energy research. Metaheuristic algorithms such as genetic algorithms (GA), differential evolution (DE), particle swarm optimization (PSO),

grey wolf optimization (GWO), and ant colony optimization (ACO), have been widely adopted due to their ability to handle complex, nonconvex objective functions. These approaches have demonstrated potential for improving in turbine wind turbine performance across various applications. Nevertheless, when applied as standalone algorithms, metaheuristics method frequently exhibit limitations, including premature convergence, sensitivity to algorithm specific parameter tuning, and limited local refinement capability near optimal solutions (Bolaños et al., 2025). Such limitations become more pronounced under low-wind tropical conditions, where wind-speed distributions are often highly variable and multimodal due to monsoonal and diurnal effects.

However, despite recent advances turbine optimization studies, several critical gaps remain for small-scale wind turbines operating in low-wind tropical regions (Karthikeyan and Hussain, 2025). Existing studies predominantly focus on utility-scale turbines or high-wind environments, with comparatively limited attention given to tropical sites characterised by low mean wind speeds. Moreover, many optimization studies rely on uncalibrated theoretical power models, which tend to overestimate achievable energy yield under low-wind condition where aerodynamic, mechanical, and electrical losses are significant (Baca et al., 2026). In addition, the robustness and repeatability of stochastic optimisation results are often insufficiently demonstrated, with limited use of multi-run statistical validation. These limitations restrict the practical applicability of existing optimization approaches for small-scale wind energy deployment in tropical regions.

To address these limitations, this study proposes a calibration-aware hybrid global–local optimization approach that integrates PSO with the L-BFGS-B algorithm for small-scale HAWTs operating under low-wind tropical conditions. The novelty of this work lies in three key aspects. First, the optimization is driven by an empirically calibrated AEP model based on multi-year ground-measured wind data, thereby reducing the systematic overestimation commonly observed in low-wind environments. Second, blade length and hub height are investigated as practically adjustable design variables, ensuring direct relevance to real-world deployment and retrofit scenarios. Third, the proposed hybrid optimization approach is evaluated across multiple geographically diverse Indonesian sites to assess its general applicability under tropical wind regimes.

Within this scope, the study focuses on establishing a practical optimization baseline for geometric parameter tuning aimed at maximizing energy yield, rather than detailed aerodynamic blade redesign or economic assessment. This targeted focus is intended to support preliminary design estimation and site-specific deployment planning for small-scale wind turbines in tropical regions.

# Methods: PSO-L-BFGS-B

## Optimization Technique

The AEP calibration and validation pipeline adopted in this study is summarized in *Fig. 1*. The workflow links probabilistic wind-speed modelling (Weibull/bi-Weibull), aerodynamic energy computation using the baseline TSD-500 power model, and empirical correction using measured AEP, followed by regression-based validation. Importantly, this structure converts multi-year AWS wind records into a calibrated AEP function $AEP_{calib}$ ($L$,$H$), which is then used as the objective function for optimizing blade length L and hub height H under low-wind tropical conditions.

Wind speed data used in this study were obtained from ground-measured automatic weather stations (AWS) deployed at five representative Indonesian locations including Jambi, South Sulawesi, West Nusa Tenggara (NTB), East Nusa Tenggara (NTT), and Maluku over the period 2017–2020. Measurements were recorded at a 10-second sampling interval at a hub height of 15 m and subsequently aggregated into hourly and daily averages for analysis. The wind datasets used in this study were obtained through institutional collaboration and are not publicly available. Since wind speed measurements were available at a reference hub height of 15 m, wind speeds at candidate hub heights up to 19 m were extrapolated using the standard power-law formulation. A uniform shear exponent of $\alpha = 0.16$ was adopted, representing tropical lowland terrain with mixed surface roughness. This value was selected as a conservative approximation to avoid artificial amplification of wind resources while maintaining physical realism across sites.

**Fig. 1.** *AEP calibration and validation workflow integrating wind data processing, probabilistic modelling, empirical correction, and validation*

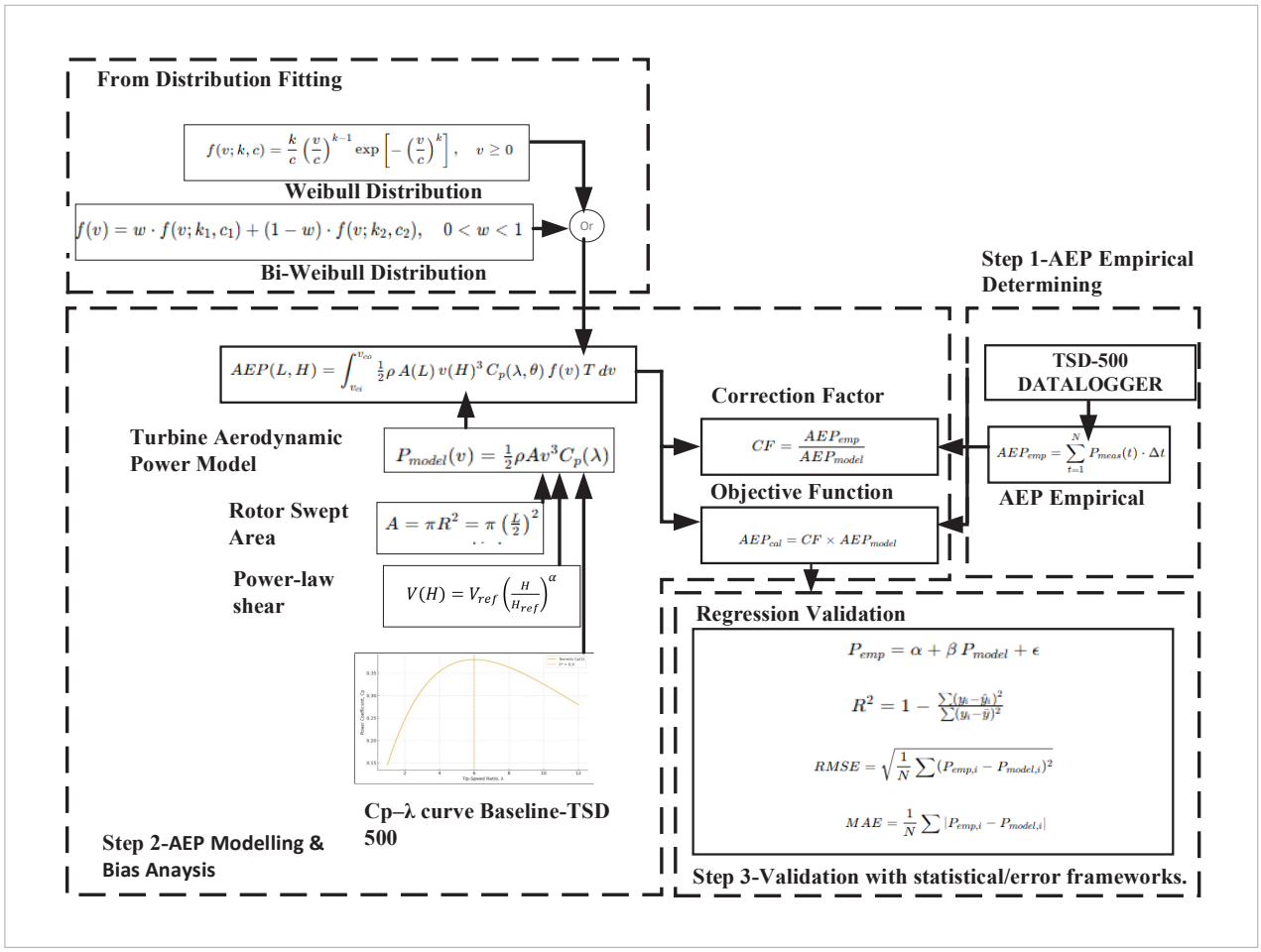


Air density was computed assuming standard tropical near-sea-level atmospheric conditions. Site-specific variations in temperature, pressure, and relative humidity were not explicitly modeled. While recent studies have demonstrated that humidity can influence air density and consequently affect wind power density and AEP estimation (Mubarok and Tian, 2022), the present study adopts an alternative strategy by implicitly accounting for such environmental effects through empirical AEP calibration. Specifically, a correction factor (Cf) derived from measured annual energy production was applied to align modeled turbine performance with real-world operation under local climatic conditions. This approach allows the optimization framework to capture the combined influence of unmodeled atmospheric factors including humidity, turbulence intensity, and electromechanical losses without introducing additional site-dependent meteorological parameters that could compromise optimization robustness and comparability across locations.

Data quality control and pre-processing were applied prior to modelling to ensure the reliability of the wind-speed datasets. Outliers were identified and removed using the interquartile range (IQR) criterion, resulting in the exclusion of approximately 2–4% of data points across the five sites. Missing values accounted for less than 1% of the total records and were treated using linear interpolation, with a maximum allowable gap of 30 minutes to preserve short-term temporal variability. All data were standardized to SI units to ensure consistency across sites prior to subsequent statistical modelling and AEP analysis.

Following data standardization and quality control, the wind speed characteristics at each site were statistically characterized to capture their inherent variability and

energy potential. This stage serves as the analytical bridge between data acquisition and energy modelling, where the two-parameter Weibull distribution was employed owing to its proven versatility in representing a wide range of wind regimes (Aras et al., 2020; Badawi et al., 2022). The probability density function (PDF) of the Weibull distribution is expressed as:

$$f(v;k,c) = \frac{k}{c}\left(\frac{v}{c}\right)^{k-1} \exp\left[-\left(\frac{v}{c}\right)^{k}\right], v \geq 0 \quad (1)$$

where $f(v; k, c)$ – probability density function (PDF) of wind speed v; $v$ – wind speed (m/s); $k$ – shape parameter (dimensionless), determines the spread of wind speed; $c$ – scale parameter (m/s), proportional to the average wind speed.

Based on the statistical wind representation, an analytical AEP model was formulated and subsequently calibrated to reconcile discrepancies between theoretical predictions and real turbine performance under low-wind tropical conditions. A site-specific correction factor, Cf was derived from measured annual energy production and applied to the modelled outputs. Model accuracy was subsequently assessed through validation using the coefficient of determination ($R^2$), root mean square error (RMSE), and mean absolute error (MAE), ensuring that the calibrated model reliably represents observed turbine behavior.

The optimization framework is developed using the TSD-500 small-scale HAWTs as the baseline reference configuration. The turbine operates within a cut-in and cut-out wind-speed range of 3–25 m/s, which defines the valid operational domain adopted in the AEP modelling. Blade length and hub height are treated as the primary optimization variables and are constrained within practical bounds to ensure physical feasibility and realistic deployment under low-wind tropical conditions. Aerodynamic and electromechanical efficiencies are not modelled explicitly; instead, their combined influence is incorporated through the empirical calibration applied to the AEP model.

While the two-parameter Weibull distribution adequately represents unimodal and relatively stable wind regimes, it may not fully capture the complex variability observed in tropical regions, where wind patterns are influenced by monsoonal and diurnal cycles. To address this limitation, a bi-Weibull distribution was adopted for sites exhibiting multimodal behavior, providing a more flexible statistical representation of the wind profile (Aldaoudeyeh, 2024; Gómez-Lázaro et al., 2016):

$$f(v) = w.f(v;k_1,c_1) + (1-w)\cdot f(v;k_2,c_2),\ 0 < w < 1 \quad (2)$$

where $f(v)$ – probability density function (PDF) of wind speed $v$; $w$ – the weighting factor; ($k_1$, $c_1$) and ($k_2$, $c_2$) – the shape and scale parameters of the two Weibull components.

The adoption of both Weibull and bi-Weibull models ensured that the probabilistic characteristics of each site were accurately represented, forming a robust foundation for subsequent energy computation. Once the statistical representation of the wind regime was established, these distributions were integrated into the aerodynamic modelling stage to estimate the extractable kinetic power available to the turbine. This transition from probabilistic modelling to energy formulation quantitatively links the stochastic nature of wind with the physical performance of the turbine (Hasan et al., 2022; Kelele et al., 2022).

Before computing aerodynamic power and integrating AEP, the wind speed must be expressed at the candidate hub height and the rotor swept area must be defined as a function of the design variable L, as indicated in the Step-2 aerodynamic block of *Fig. 1*. Since AWS measurements were available at the reference height $H_{ref}$=15 m, the wind speed at a candidate hub height H was extrapolated using the power-law wind shear model:

$$V(H) = V_{ref}\left(\frac{H}{H_{ref}}\right)^{\alpha} \quad (3)$$

where $V_{ref}$ – measured wind speed at the reference height (m/s); $H_{ref}$ – height of tower; H – candidate hub height; and $\alpha$ – wind shear exponent.

A uniform $\alpha$=0.16 was adopted as a conservative approximation for tropical lowland terrain with mixed roughness. The rotor swept area was then expressed directly in terms of blade length. For a horizontal-axis rotor, the blade length corresponds to the rotor radius (R=L), hence:

$$A = \pi R^2 = \pi L^2 \quad (4)$$

where A - rotor swept area ($m^2$); R - rotor radius (m); and L - blade length.

With and A(L) defined, the instantaneous aerodynamic power extracted from the wind is computed using the standard turbine power formulation (central power-model block in *Fig. 1*):

$$P(V(H), L) = \frac{1}{2}\rho A(L) C_p(\lambda) V(H)^3 \quad (5)$$

where $P(V(H), L)$ – power output of turbine (W); $\rho$ – air density (kg/m$^3$); $A(L)$ – rotor swept area as a function of blade length (m$^2$); $Cp(\lambda)$ – power coefficient as a function of tip speed ratio (dimensionless); $V(H)$ – wind speed at hub height (m/s).

In this study, λ (and thus *Cp*) is not optimized explicitly; it is embedded in the baseline TSD-500 performance representation and subsequently corrected through empirical calibration.

The instantaneous power output expressed in Equation (5) represents the kinetic energy conversion at a given wind speed. However, wind speed varies continuously throughout the year, and the turbine operates only within specific limits defined by the cut-in and cut-out velocities. Therefore, to evaluate the total energy yield under realistic operating conditions, the power curve must be integrated over the site-specific wind-speed probability distribution. This integration yields the expected AEP, as formulated in (Mubarok and Tian, 2022; Sumair et al., 2021):

$$AEP_{model}(L,H) = \int_{v_{ci}}^{v_{co}} P(V,L,H) f(V) d \times T \quad (6)$$

where $AEP_{model}$ ($L$, $H$) – modelled annual energy production (kWh); $V_{ci}$ – cut-in wind speed (m/s); $V_{\infty}$ – cut-out wind speed (m/s); $T$ – total number of hours in a year (8760 h); $f(V)$ – probability density function of wind speed; L – length of blades (m); H – heigh of wind turbine (m).

Although analytical integration of the power equation is possible for simple parametric distributions such as the Weibull distribution, this study adopts a numerical integration approach to ensure methodological consistency across all fitted probability models, including the bi-Weibull distribution. AEP was computed by numerically integrating the turbine power output weighted by the fitted wind-speed probability density function over discretized wind-speed bins. Wind speed was discretized using fixed-width bins derived from the empirical distribution, and numerical integration was performed using a trapezoidal scheme. Numerical convergence was verified by refining the discretization until the resulting change in AEP was below 0.1%.

This integration enables a realistic estimation of the turbine's long-term energy yield by coupling aerodynamic behavior with the stochastic nature of wind variability. Although Equation (6) provides a theoretical estimate of annual energy output, discrepancies often arise between simulated and real-world performance due to aerodynamic, mechanical, and electrical losses. To address this, an empirical calibration was applied through a correction factor, computed as the ratio between measured and modelled annual energy production, thereby aligning theoretical predictions with observed performance:

$$Cf = \frac{AEP_{emp}(L,H)}{AEP_{model}(L,H)} \quad (7)$$

where $Cf$ – correction factor (dimensionless); $AEP_{model}$ (L,H) – empirical annual energy production (kWh); $AEP_{model}$ (L,H) – modelled annual energy production (kWh).

The calibrated annual energy production, $AEP_{calib}$ was subsequently obtained by applying the correction factor, thereby reconciling modelled and observed performance:

$$AEP_{calib}(L,H) = Cf \cdot AEP_{model}(L,H) \quad (8)$$

where $Cf$ – correction factor (dimensionless); $AEP_{calib}$ ($L$, $H$) – calibrated annual energy production (kWh); $AEP_{model}$ ($L$, $H$) – modelled annual energy production (kWh).

This calibration ensures that the energy model remains physically realistic under low-wind tropical and monsoonal conditions, where conventional theoretical formulations tend to overestimate energy yield. The correction factor implicitly accounts for aggregated aerodynamic, mechanical, and electrical losses that are not explicitly represented in idealized models.

The optimization in this study focuses on maximizing calibrated annual energy production through geometric and site-related parameters rather than aerodynamic blade redesign. Accordingly, the power coefficient (Cp) and tip-speed ratio (TSR) are not treated as explicit optimization variables. As no blade profile or rotational control parameters are modified, the Cp –TSR characteristics of the optimized configurations

remain identical to those of the baseline rotor and are therefore not explicitly reported.

Model performance was subsequently validated using standard statistical indicators including R2, RMSE, and MAE to assess predictive accuracy and reliability (Douiri, 2024; Ndeba et al., 2025):

$$RMSE = \sqrt{\frac{1}{n}\sum_{i=1}^{n}(P\ Model,i - P\ Emprical,i)^2} \quad (9)$$

where *RMSE* – root mean squared error (W); *P Emprical*, *i* – empirical power output (W); *P Model*, *i* – modelled power output (W).

$$MAE = \frac{1}{n}\sum_{i=1}^{n}|P\ Model,i - P\ Empirical,i| \quad (10)$$

where *MAE* – mean absolute error (W); *P Empirical* – empirical power output (W); *P Model* – modelled power output (W).

$$R^2 = 1 - \frac{\sum_{i=1}^{n}(yi-\widehat{yi})^2}{\sum_{i=1}^{n}(yi-\overline{yi})^2} \quad (11)$$

where $R^2$ – Coefficient of determination; $yi$ – empirical values; $\widehat{yi}$ – predicted values; $\overline{yi}$ – mean of empirical values.

A high determination coefficient $R^2 > 0.97$ and low RMSE or MAE values confirmed the model's fidelity in reproducing empirical turbine performance. Such validation approaches have been widely employed in wind-energy modelling to verify the robustness of integrated probabilistic–aerodynamic frameworks.

Collectively, *Fig. 1* synthesizes the integrated methodological sequence linking data preprocessing, probabilistic distribution fitting, empirical calibration, and statistical validation thus providing a consistent and validated foundation for the subsequent optimization of blade length (L) and hub height (H). PSO was implemented using a swarm size of 30 particles and a maximum of 600 iterations per site. The inertia weight was linearly decreased from 0.9 to 0.4 to balance exploration and exploitation, while the cognitive and social acceleration coefficients were set to $c_1 = c_2 = 2.0$. Particle positions were constrained within the predefined design space of blade length $L \in [1.5,2.0]$ m and hub height $H \in [10,20]$ m. Velocity clamping was applied to limit particle velocities to ± 20% of the corresponding variable range to avoid unstable oscillations.

Building on the calibrated energy model established in *Fig. 1*, *Fig. 2* illustrates the proposed hybrid PSO–L-BFGS-B optimization framework used to maximize the calibrated annual energy production $AEP_{calib}$ (*L*, *H*).

The left section of *Fig. 2* represents the global exploration phase, where PSO particles search the two-dimensional design space defined by blade length and hub height. Each particle corresponds to a candidate turbine configuration evaluated using the calibrated AEP objective function.

After PSO convergence, the best global solution (gbest) is transferred to the L-BFGS-B stage, shown in the right section of *Fig. 2*. In this local refinement phase, gradient information is approximated using finite differences, and the solution is iteratively improved through line-search steps under box constraints. This sequential coupling enables the algorithm to retain PSO's global search capability while benefiting from the fast local convergence of L-BFGS-B.

The hybrid coupling adopts a sequential two-stage strategy in which L-BFGS-B is invoked once after PSO convergence, using the final global best particle as the initial condition. This approach preserves PSO's global search capability while improving local optimality. All simulations were executed on a standard desktop workstation (Intel i7 CPU, 32 GB RAM), with average wall-clock times of approximately 4–7 minutes for PSO and 6–9 minutes for the hybrid PSO–L-BFGS-B per optimisation run, demonstrating the computational feasibility of the proposed framework. The swarm updates its velocity and position iteratively according to the canonical PSO equations (Hafez and Dhaouadi, 2023):

$$v_i^{(t+1)} = wv_i^{(t)} + c_1 r_1\left(pbest_i^{(t)} - x_i^{(t)}\right) + \\ + c_2 r_2\left(gbest^{(t)} - x_i^{(t)}\right),\ x_i^{(t+1)} = x_i^{(t)} + v_i^{(t+1)} \quad (12)$$

where $c_i$ (*t*) – velocity of particle *i*; $x_i$ (*t*) – position of particle iii representing (L, H); w – inertia weight; $c_1$ $c_2$ – cognitive and social coefficients; $r_1$ $r_2$ – uniformly distributed random numbers in [0,1]; $pbest^{(t)}$ – individual best position; $gbest^{(t)}$ – global best position.

Once the global exploration converges, the best-performing particle (gbest) serves as the initial point for the L-BFGS-B refinement stage, as shown in the right panel of *Fig. 2*. The L-BFGS-B algorithm evaluates both the objective and its gradient ∇J(x) using finite-difference approximation and updates search directions via a two-loop recursion. A line-search procedure satisfying the Armijo–Wolfe conditions ensures stable descent,

**Fig. 2.** *Proposed hybrid PSO–L-BFGS-B optimization framework: global search using PSO over blade length and hub height, followed by local refinement using L-BFGS-B with finite-difference gradients, line-search (Armijo–Wolfe), and bound projection to obtain the final optimized configuration*

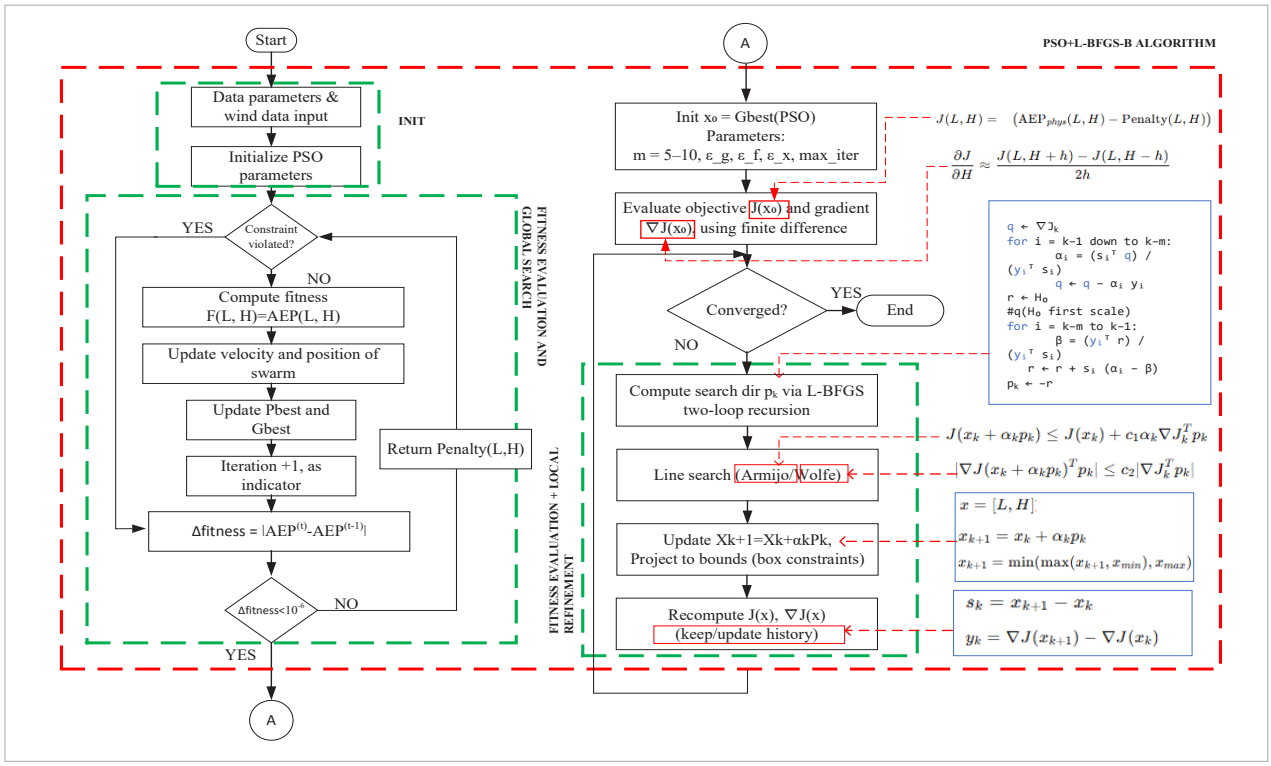


(Li and Bai, 2024) while box constraints are enforced through projection operators at each step:

$$x^* = L - BFGS - B\ (Objective = \\ = -AEP_{cal}(L,H), init = x_{pso}, bounds) \quad (13)$$

where $x^*$ – refined solution; $x_{pso}$ – best solution obtained from PSO.

This hybrid integration allows PSO to identify promising global regions, while L-BFGS-B exploits local curvature information to achieve rapid convergence toward the true optimum.

To ensure reliability and reproducibility, both algorithms were executed with randomized initializations. The best-so-far annual energy production at iteration k is tracked as:

$$AEP^*(k) = \max_{i=1,..,n} AEP(xi) \quad (14)$$

where $AEP^*(k)$ – best *AEP* at iteration *k*; $AEP(xi)$ – AEP obtained from solution i; *n* – number of particles or runs.

Collectively, *Fig. 2* summarizes the hybrid optimization process, where PSO performs global exploration and L-BFGS-B provides local refinement to obtain the final optimized turbine configuration.

To verify the stability and statistical significance of the optimized solutions, a robustness and validation stage was subsequently implemented, as illustrated in *Fig. 3*. This stage comprised two sequential procedures: robustness testing through repeated simulation runs and statistical validation using non-parametric hypothesis testing. In the robustness analysis (left section of *Fig. 3*), the hybrid PSO–L-BFGS-B framework was executed across 30 independent Monte Carlo runs for each site using randomized initial swarm configurations. This repetition was intended to capture the stochastic variability inherent to metaheuristic algorithms and to evaluate convergence stability under different initialization scenarios. The results from these multiple runs yielded distributions of the AEP for both PSO and Hybrid configurations. Descriptive indicators such as the median and IQR were computed to assess central

**Fig. 3.** *Robustness and statistical validation framework: 30-run Monte Carlo robustness analysis producing AEP distributions for PSO and hybrid PSO–L-BFGS-B; Mann–Whitney U-test procedure for statistical comparison of algorithm performance*

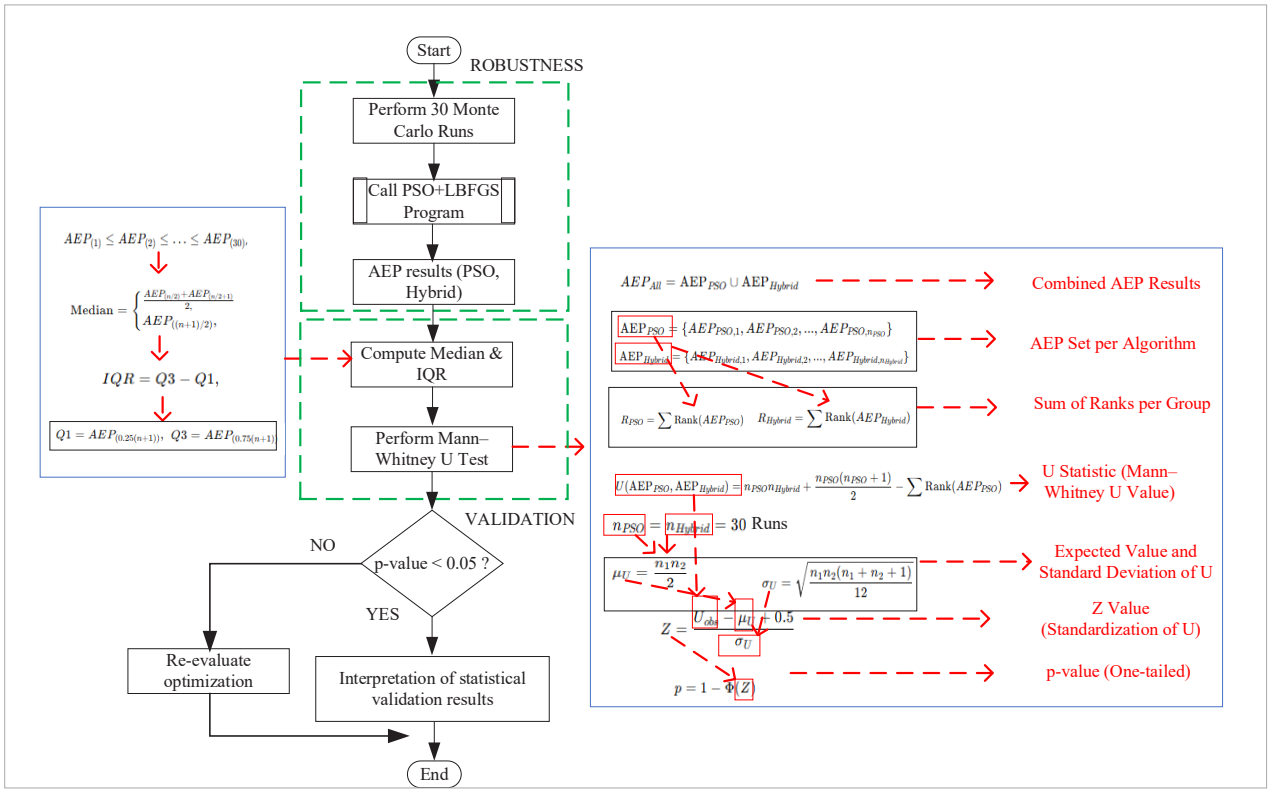


tendency and dispersion, respectively, providing quantitative measures of consistency and reliability.

Subsequently, statistical validation (right section of *Fig. 3*) was performed to determine whether the performance improvements of the hybrid method were statistically significant. The Mann–Whitney U-test, a non-parametric rank-based test, was employed due to its robustness against non-normal data distributions. The combined dataset was ranked, and the U-statistic was computed as:

$$U(AEP_{pso}, AEP_{hybrid}) = n_{PSO}n_{Hybrid} + + \frac{n_{PSO}(n_{PSO}+1)}{2} - \sum Rank(AEP_{PSO}) \quad (15)$$

where: $n_{PSO}$ $n_{Hybrid}$ – represent the number of observations for each algorithm;

The corresponding Z-value and p-value were derived to test the null hypothesis, which

$H_0$: "there is no significant difference between PSO and Hybrid performance."

A significance threshold of $p < 0.05$ was adopted to confirm meaningful improvement. If the null hypothesis was rejected ($p < 0.05$), the hybrid optimization results were deemed statistically superior and robust. Otherwise, the optimization parameters were re-evaluated to verify convergence stability. This rigorous two-tier evaluation ensured that performance improvements were not merely artifacts of random initialization but reflected genuine algorithmic enhancements.

Overall, the robustness and validation framework illustrated in *Fig. 3* reinforces the methodological reliability of the study, ensuring that the hybrid PSO–L-BFGS-B approach achieves statistically validated, reproducible, and physically consistent optimization outcomes across all evaluated sites.

## Results and Discussion

The wind regimes at the five investigated locations were analysed to establish the probabilistic basis for

subsequent AEP modelling and optimisation. The geographic distribution and elevation of the measurement sites are summarised in *table 1*, highlighting the diverse climatic and topographical conditions across the Indonesian archipelago. Based on long-term wind-speed records from 2017 to 2020, Weibull and bi-Weibull distributions were fitted to the empirical data to capture site-specific wind characteristics under low-wind and heterogeneous regimes.

*Table 2* reveal distinct wind-speed profiles across the study sites. For instance, Western Indonesian locations such as Jambi and Sulawesi exhibit relatively low scale parameters (c ≈ 3–5 m/s) and shape parameters close to unity, indicating weak but comparatively uniform wind conditions. These characteristics suggest that performance improvements in such regions are more effectively achieved through increased hub height rather than extended blade length, as accessing stronger wind layers provides greater marginal gains than enlarging the rotor-swept area.

In contrast, eastern Indonesian sites, including NTT, NTB, and Maluku, are better represented by bi-Weibull distributions characterised by two distinct components, with lower-speed regimes (c1 ≈ 4–5 m/s) and higher-speed regimes (c2 ≈ 7–9 m/s). This behaviour reflects the influence of seasonal monsoonal patterns, where low-speed winds dominate during the west monsoon and higher-speed winds occur during the east monsoon. For these locations, turbine configurations must accommodate both operating regimes, favouring a combination of moderate hub heights and increased blade lengths to capture the available energy across the full wind-speed spectrum.

The goodness-of-fit of the Weibull and bi-Weibull distributions was evaluated using the Kolmogorov-Smirnov (K–S) test and the Bayesian Information Criterion (BIC), as summarized in *table 3*. The K–S p-values provide a statistical indication of the agreement between empirical and modelled wind-speed distributions, while BIC is used as the primary criterion for distribution selection to account for differences in model complexity.

**Table 1.** *Geographic coordinates and elevation of AWS measurement sites*

| Location | Latitude (°) | Longitude (°) | Elevation (m a.s.l.) |
|---|---|---|---|
| Maluku | 2.5619 | 128.6278 | 38 |
| Jambi | –1.3486 | 104.4561 | 1 |
| Sulawesi | –5.6327 | 119.7749 | 75 |
| NTB | –8.9165 | 116.4574 | 7 |
| NTT | –10.3547 | 123.7319 | 2 |

Based on the combined validation results, the suitability of the probability distributions is site-dependent. The bi-Weibull distribution yields lower BIC values for NTT, NTB, and Maluku, indicating that the additional model flexibility is justified for these locations, which exhibit more complex or multimodal wind-speed characteristics. In contrast, the standard Weibull distribution is sufficient to describe the wind-speed characteristics of Sulawesi and Jambi, as reflected by its lower BIC values. The selected distributions are further supported by comparisons between empirical and fitted probability density and cumulative distribution functions, as illustrated in *Fig. 4*, and are subsequently used for AEP modelling.

This section presents the outcomes of model calibration, optimization performance, and comparative evaluation. The calibration step was essential to ensure that the analytical energy model used for optimization

**Table 2.** *Estimated parameters of Weibull and Bi-Weibull wind-speed distributions for the five study locations based on 2017–2020 measurements*

| Locations | Weibull | | Bi-Weibull | | | | |
|---|---|---|---|---|---|---|---|
| | k | c | W | k1 | c1 | k2 | c2 |
| Sulawesi | 2.122 | 5.091 | 0.902 | 2.17 | 4.846 | 2.7 | 7.302 |
| NTT | 2.653 | 6.701 | 0.274 | 3.04 | 6.011 | 2.62 | 6.951 |
| NTB | 1.94 | 4.908 | 0.865 | 1.99 | 4.571 | 2.44 | 7.078 |
| Maluku | 2.417 | 5.828 | 0.943 | 2.51 | 5.6 | 4.13 | 9.285 |
| Jambi | 1.479 | 3.402 | 0.665 | 1.5 | 2.98 | 1.61 | 4.282 |

**Table 3.** *Validation metrics for distribution selection (2017–2020)*

| Locations | Weibull | | Bi-Weibull | |
|---|---|---|---|---|
| | K–S p-value | BIC | K–S p-value | BIC |
| Sulawesi | 0.0937 | 152753.9 | 0.989 | 152758 |
| NTT | 0.0173 | 160034.9 | 0.9833 | 160010.9 |
| NTB | 0.034 | 154666.0 | 0.8565 | 154662.9 |
| Maluku | 0.1142 | 155317.6 | 0.5632 | 155298.4 |
| Jambi | 0.1451 | 141593.7 | 0.8066 | 141610.0 |

accurately reflects the real operating behavior of the baseline TSD-500 turbine. Establishing this alignment improves the credibility of subsequent optimization of blade length (L) and hub height (H) for energy maximization.

The calibration results demonstrated that the unadjusted model systematically overestimated the measured AEP by 17–31% across all sites during 2017–2020 (*table 4* and *Fig. 5*). Applying the site-specific correction factor Cf effectively removed the bias, with post-calibration values closely matching the 1:1 reference line. Regression validation (*table 5*) confirmed a strong correlation between calibrated and measured outputs, yielding.

$R^2$ = 0.85–0.90, RMSE ≤ ~12% rated power, and slopes approaching unity with minimal intercepts. These results verify that the calibrated energy function $AEP_{cal}$ (L, H) is both physically consistent and statistically reliable for use in the hybrid PSO–L-BFGS-B optimisation stage.

*Table 5* was reformatted to clearly separate absolute error metrics (RMSE and MAE in Watt) from their normalized counterparts expressed as percentages of

**Table 4.** *Comparison of empirical and modelled AEP and derived site-specific correction factors (2017–2020)*

| Locations | AEP (kWh/year) | | | CF | Overestimate |
|---|---|---|---|---|---|
| | Empirical | Modelled | Calibrated | | |
| Jambi | 318.6 | 419.3 | 318.6 | 0.76 | 31.60% |
| Maluku | 920 | 1130.2 | 920 | 0.81 | 22.80% |
| NTB | 655.4 | 823.1 | 655.4 | 0.80 | 25.60% |
| NTT | 1223.2 | 1477 | 1223.2 | 0.83 | 20.80% |
| Sulawesi | 740.4 | 868.5 | 740.4 | 0.85 | 17.30% |

**Fig. 4.** *Empirical wind-speed histograms for the five study locations: (a) Maluku, (b) Jambi, (c) Sulawesi, (d) NTB, (e) NTT*

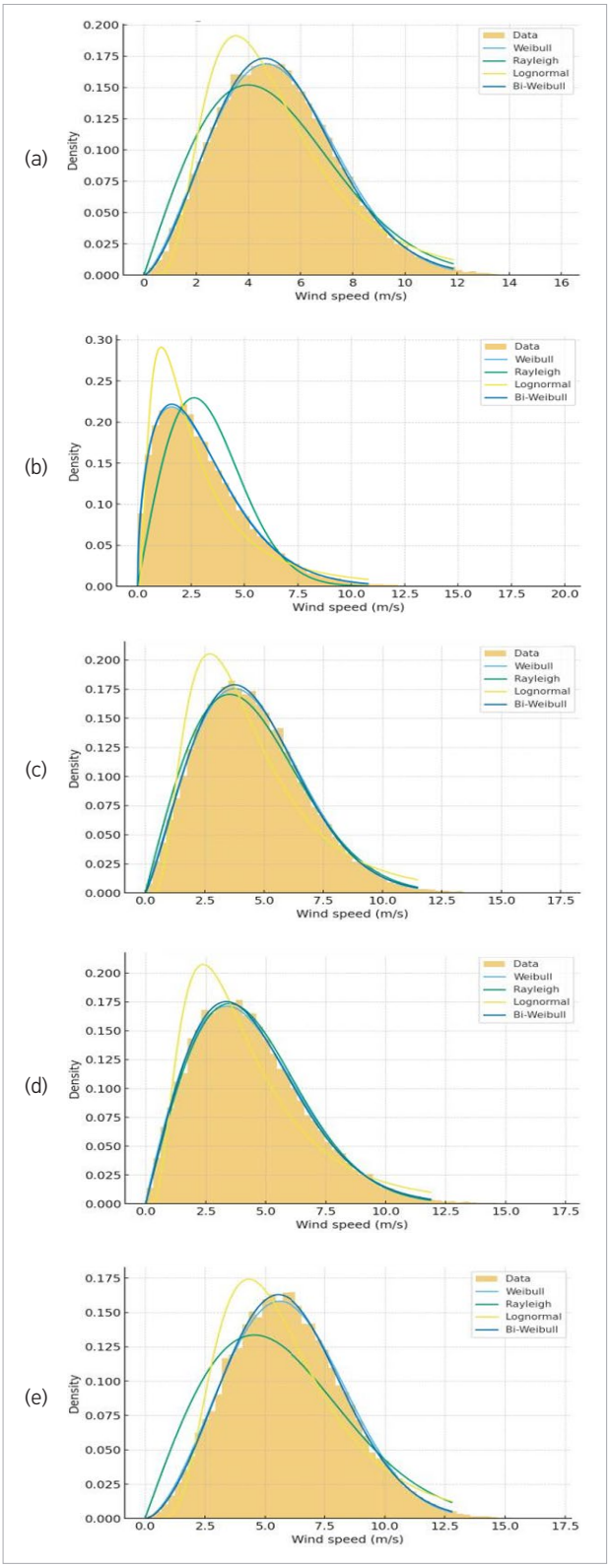

**Fig. 5.** *Regression-based validation of calibrated modelled power against empirical measurements for the five study locations: (a) Before calibration (b) After calibration*

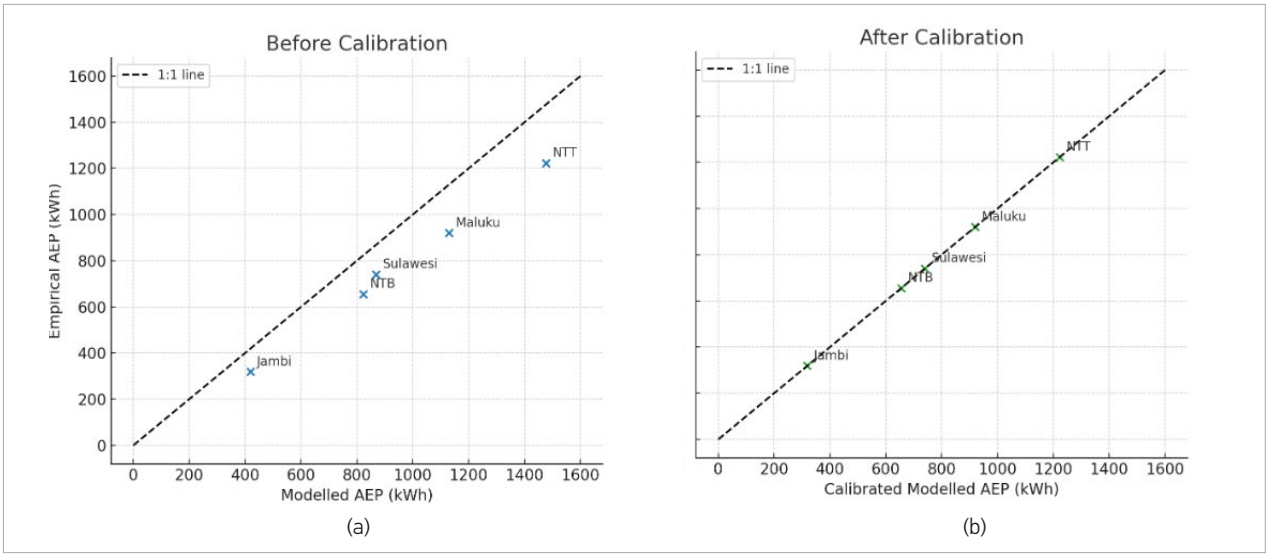


rated power, thereby eliminating redundancy and improving cross-site comparability. Across all locations, the calibrated model exhibits strong agreement with measured power output, with coefficients of determination ranging from $R^2$ = 0.85 to 0.90 and regression slopes generally close to unity. Although the regression slope for Jambi (0.856) is below unity, the corresponding $R^2$ remains high (0.898), indicating strong linear correlation. This slope deviation reflects mild systematic underestimation at higher power levels, which is characteristic of low-wind regimes where turbine operation is concentrated near cut-in conditions and power variability is compressed.

The relatively low RMSE and MAE values, both in absolute terms and as percentages of rated power, confirm that the calibration procedure effectively reduces modelling bias. On this basis, the calibrated annual energy production function L, H) was adopted as the objective function for the subsequent optimization stage, in which conventional PSO and the hybrid PSO–L-BFGS-B algorithms were evaluated to identify optimal blade length and hub height configurations.

With the calibration successfully aligning the theoretical and empirical energy outputs, the validated L, H) function provided a reliable foundation for the optimization stage. By ensuring that model predictions accurately represented the TSD-500's real performance under tropical low-wind conditions, subsequent optimization could focus solely on enhancing aerodynamic efficiency rather than compensating for model bias. The following section applies the calibrated objective function within the proposed hybrid optimization framework combining the global exploration capability of PSO and the local convergence precision of L-BFGS-B to identify the optimal L and H configurations that maximize site-specific annual energy yield.

**Table 5.** *Regression validation of calibrated modelled power against measurements*

| Locations | R2 | RMSE (Watt) | MAE (Watt) | RMSE (% rated) | MAE (% rated) | Slope | Intercept |
|---|---|---|---|---|---|---|---|
| Sulawesi | 0.901 | 37.869 | 24.132 | 7.57% | 4.83% | 0.999 | −14.506 |
| NTT | 0.852 | 59.682 | 41.973 | 11.94% | 8.40% | 1.008 | −30.263 |
| NTB | 0.885 | 41.828 | 25.712 | 8.37% | 5.14% | 0.927 | −12.269 |
| Maluku | 0.893 | 45.864 | 33.06 | 9.17% | 6.61% | 0.99 | −22.742 |
| Jambi | 0.898 | 29.392 | 14.342 | 5.88% | 2.87% | 0.856 | 4.586 |

Following the successful calibration, the validated energy function was applied within the optimization framework to evaluate two algorithms: the conventional PSO and its hybrid extension PSO-L-BFGS-B. Building on the validated L, H) model, the optimization process was executed to determine the turbine configurations that maximize annual energy yield across the five study sites with distinct wind characteristics.

*Fig. 6* presents the convergence trajectories for PSO and Hybrid PSO–L-BFGS-B. Interestingly, the standard PSO demonstrated a faster early-stage convergence, reaching its plateau after approximately 150–250 iterations, while the hybrid algorithm required more evaluations around 400–500 iterations to stabilize. However, although PSO converged more quickly, its solutions tended to stagnate at lower L, H) values. In contrast, the hybrid algorithm continued improving gradually, ultimately achieving higher and more stable energy outputs at convergence. This behavior reflects the expected trade-off: PSO favors rapid exploration, while the hybrid method expends additional iterations in local refinement via L-BFGS-B to reach a superior optimum.

The optimised blade length and hub height configurations, together with the corresponding calibrated AEP values, are summarised in *table 6*. Relative to the baseline TSD-500 configuration, both optimisation methods yield improvements in annual energy production, with the hybrid algorithm achieving higher gains at all locations.

*Table 7* summarizes the optimized H and D obtained from the PSO and hybrid PSO-L-BFGS-B solutions for each study site. Relative to the baseline configuration (H = 15 m, D = 3.0 m), both optimization methods result in increased hub heights and rotor diameters across all locations. The hybrid PSO-L-BFGS-B consistently selects higher hub heights than the standard PSO, while the optimized rotor diameters remain within a narrow range of 3.8–4.0 m for all sites.

The optimization results indicate that blade length increased from 1.5 m to 1.9–2.0 m and hub height increased from 15 m to 17–19 m across all study sites. Compared with the standard PSO, the hybrid PSO–L-BFGS-B consistently produced higher calibrated annual energy production, AEP calib (L, H), in all locations.

To evaluate the stability of these outcomes, both algorithms were further assessed using 30 independent optimization runs per site. As shown in *Fig. 7*, the distributions of AEP calib obtained from the repeated runs exhibit higher median values and narrower interquartile ranges for the hybrid method compared with PSO. The Mann–Whitney U-test confirms that the differences between the two algorithms are statistically significant ($p < 0.01$) for all sites.

**Table 7.** *Optimized hub height and rotor diameter derived from PSO and hybrid PSO-L-BFGS-B solutions*

| Locations | Method | Hub Height, H (m) | Rotor Diameter, D (m) |
|---|---|---|---|
| Maluku | PSO | 10.2 | 4.0 |
| | Hybrid | 17 | 3.8 |
| Jambi | PSO | 10.0 | 4.0 |
| | Hybrid | 19 | 4.0 |
| Sulawesi | PSO | 10.3 | 4.0 |
| | Hybrid | 18 | 3.9 |
| NTB | PSO | 10.4 | 4.0 |
| | Hybrid | 17.5 | 3.85 |
| NTT | PSO | 10.2 | 4.0 |
| | Hybrid | 16.8 | 3.8 |

**Table 6.** *Comparative statistical summary of PSO and PSO–L-BFGS-B results across five sites*

| Locations | Length and Height (meter) | | | AEP (kWh/year) | | | Baseline versus (%) | |
|---|---|---|---|---|---|---|---|---|
| | Base | PSO | Hybrid | Base | PSO | Hybrid | PSO | Hybrid |
| Jambi | (1.5, 15.0) | (2.00, 10.0) | (2.00, 19) | 318.6 | 367.1 | 397.8 | 15.20 | 24.8 |
| Maluku | (1.5, 15.0) | (2.00, 10.2) | (1.90, 17) | 920 | 977.5 | 1027.2 | 6.20 | 11.6 |
| NTB | (1.5, 15.0) | (2.00, 10.4) | (2.00, 16) | 655.4 | 671.8 | 775.9 | 2.50 | 18.4 |
| NTT | (1.5, 15.0) | (2.00, 10.2) | (1.95, 18) | 1223.2 | 1254.3 | 1419.8 | 2.50 | 16.1 |
| Sulawesi | (1.5, 15.0) | (2.00, 10.3) | (1.95, 18) | 740.4 | 794.1 | 911.2 | 7.30 | 23.1 |

**Fig. 6.** *Median convergence of PSO and Hybrid: (a) Maluku, (b) Jambi, (c) Sulawesi, (d) NTB, (e) NTT*

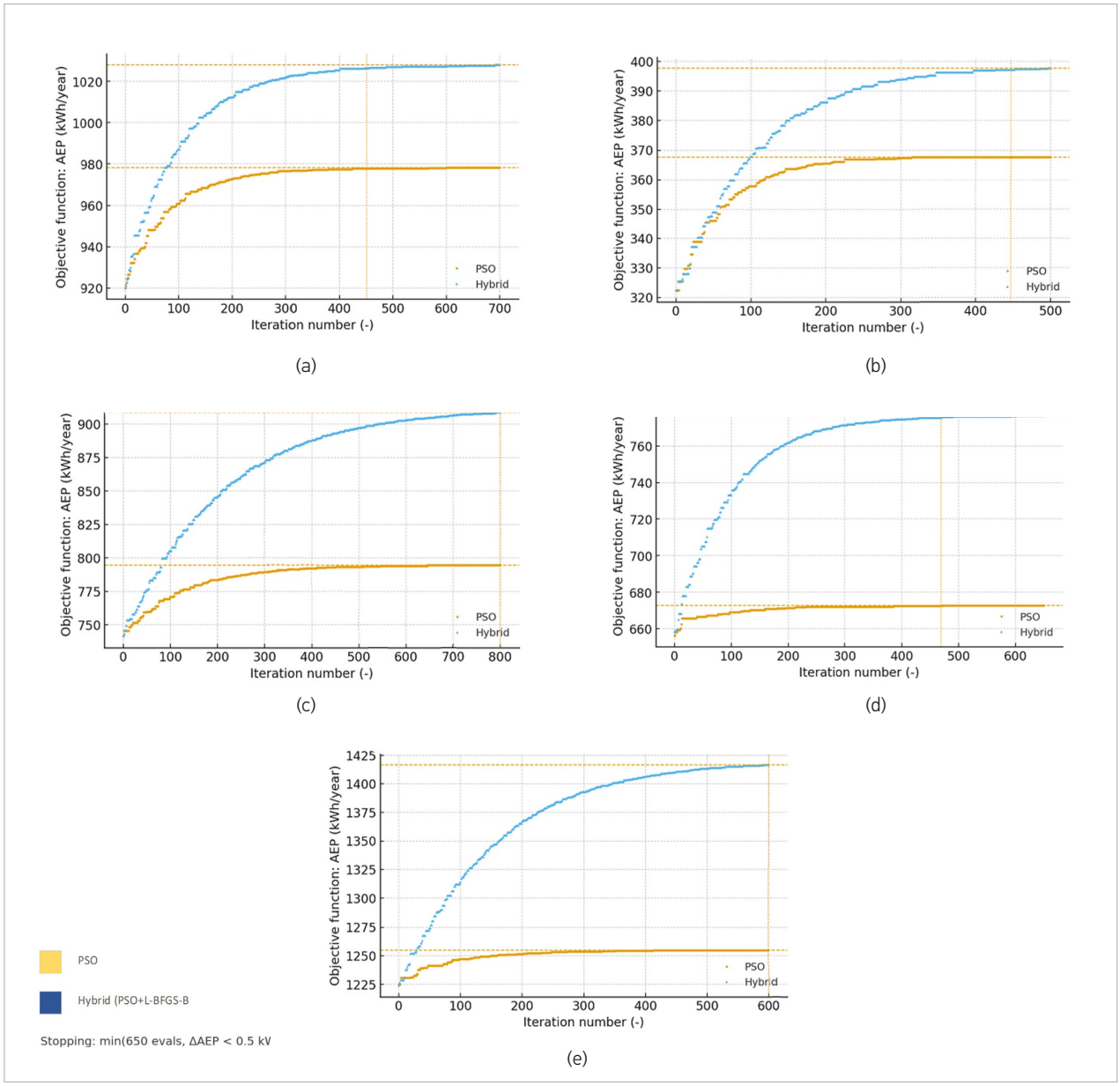


Across all five locations, the hybrid PSO–L-BFGS-B algorithm consistently achieved higher median AEP values than the standalone PSO. In most cases, this improvement is accompanied by a narrower IQR, indicating enhanced robustness. An exception is observed at the Sulawesi site, where the hybrid framework exhibits a slightly wider IQR. This behavior is attributed to the presence of a strong local optimum already well captured by PSO under relatively stable wind conditions. The gradient-based refinement stage therefore explores a broader neighborhood around the optimum without compromising median performance, reflecting exploratory refinement rather than convergence instability.

Importantly, despite the wider IQR at Sulawesi, the hybrid algorithm still delivers a substantially higher median AEP, indicating that the increased spread reflects exploratory refinement rather than convergence instability. To quantitatively support the distributional trends observed in *Fig. 7*. While *table 8* summarizes the median AEP and IQR for both algorithms.

**Fig. 7.** *Distributions of calibrated AEP values obtained from 30 independent optimization runs: (a) Maluku, (b) Jambi, (c) Sulawesi, (d) NTB, and (e) NTT*

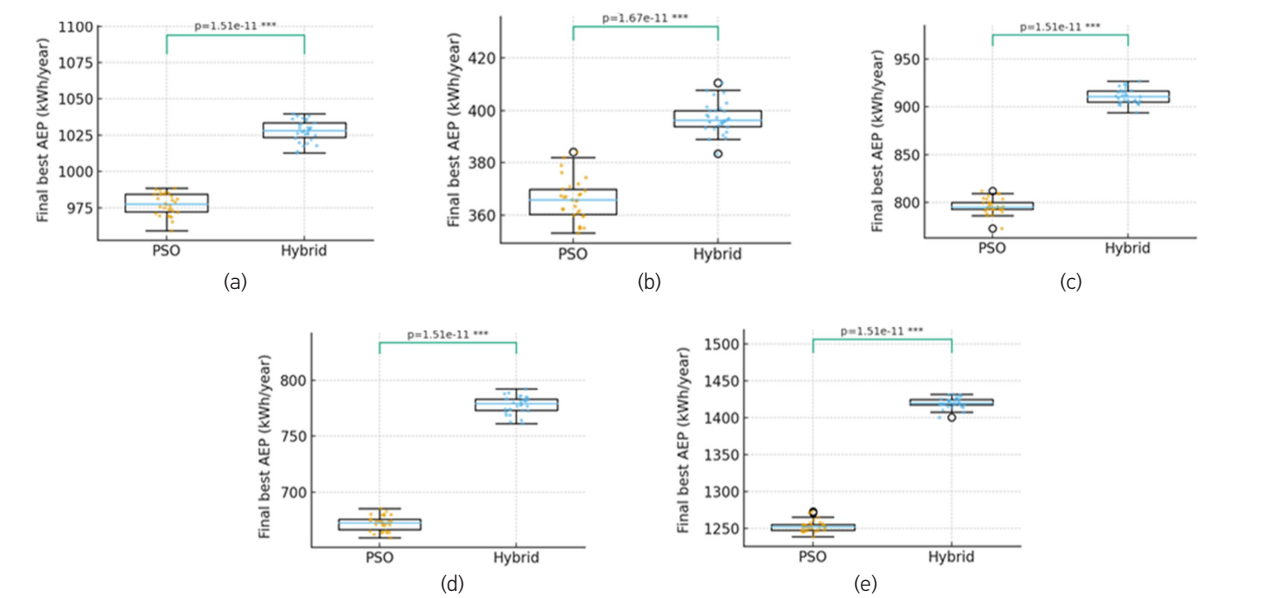


Complementary evidence is provided in *Fig. 8*, it presents the distributions of optimal blade length and hub height combinations obtained from 30 independent optimization runs for each study site. Clear clustering patterns are observed in the design space, where the hybrid PSO–L-BFGS-B consistently converges toward higher hub heights with moderate blade-length adjustments, while the standalone PSO exhibits wider dispersion. The more compact clusters produced by the hybrid approach indicate improved solution stability and reduced sensitivity to local optima. These results confirm that hub height is the dominant optimization variable under low-wind tropical conditions.

The sensitivity analysis indicates that hub height has a more pronounced influence on annual energy production than blade length across all investigated sites. While blade length adjustments contribute to incremental performance gains, variations in hub height consistently yield larger marginal increases in calibrated AEP under low-wind tropical conditions. This behavior reflects the importance of accessing stronger and more stable wind layers at higher elevations, which becomes particularly critical in regions characterized by low mean wind speeds and high temporal variability.

A clearer site-specific interpretation can be drawn from the clustering patterns in *Fig. 8*. In Maluku (*Fig. 8a*), both PSO and hybrid solutions converge toward similar blade-length ranges, while the hybrid solutions consistently select higher hub heights with tighter clustering, indicating a stable optimum under relatively steady wind conditions. In Jambi (*Fig. 8b*), a more pronounced separation between PSO and hybrid clusters is observed, where PSO solutions remain scattered across the design space, whereas the hybrid algorithm converges toward a well-defined region characterized by simultaneously increased blade length and hub height. A similar but more compact behavior is evident in South Sulawesi (*Fig. 8c*), where the hybrid solutions form a dense cluster around higher hub-height values, confirming reduced sensitivity to initialization and improved convergence stability. In NTB (*Fig. 8d*), the hybrid framework again yields a concentrated optimum region, while PSO exhibits wider dispersion, particularly along the blade-length dimension. Finally, in NTT (*Fig. 8e*), despite the relatively stable baseline configuration, the hybrid solutions consistently migrate toward higher hub heights with minimal spread, demonstrating robust convergence even in sites with less pronounced variability.

Overall, the tighter clustering of optimal hub height compared to blade length suggests a more stable and well-defined optimum across all locations. In combination with the robustness analysis, these results demonstrate that

**Fig. 8.** *Optimal design from 30 runs: a) Maluku, (b) Jambi, (c) Sulawesi, (d) NTB, (e) NTT*

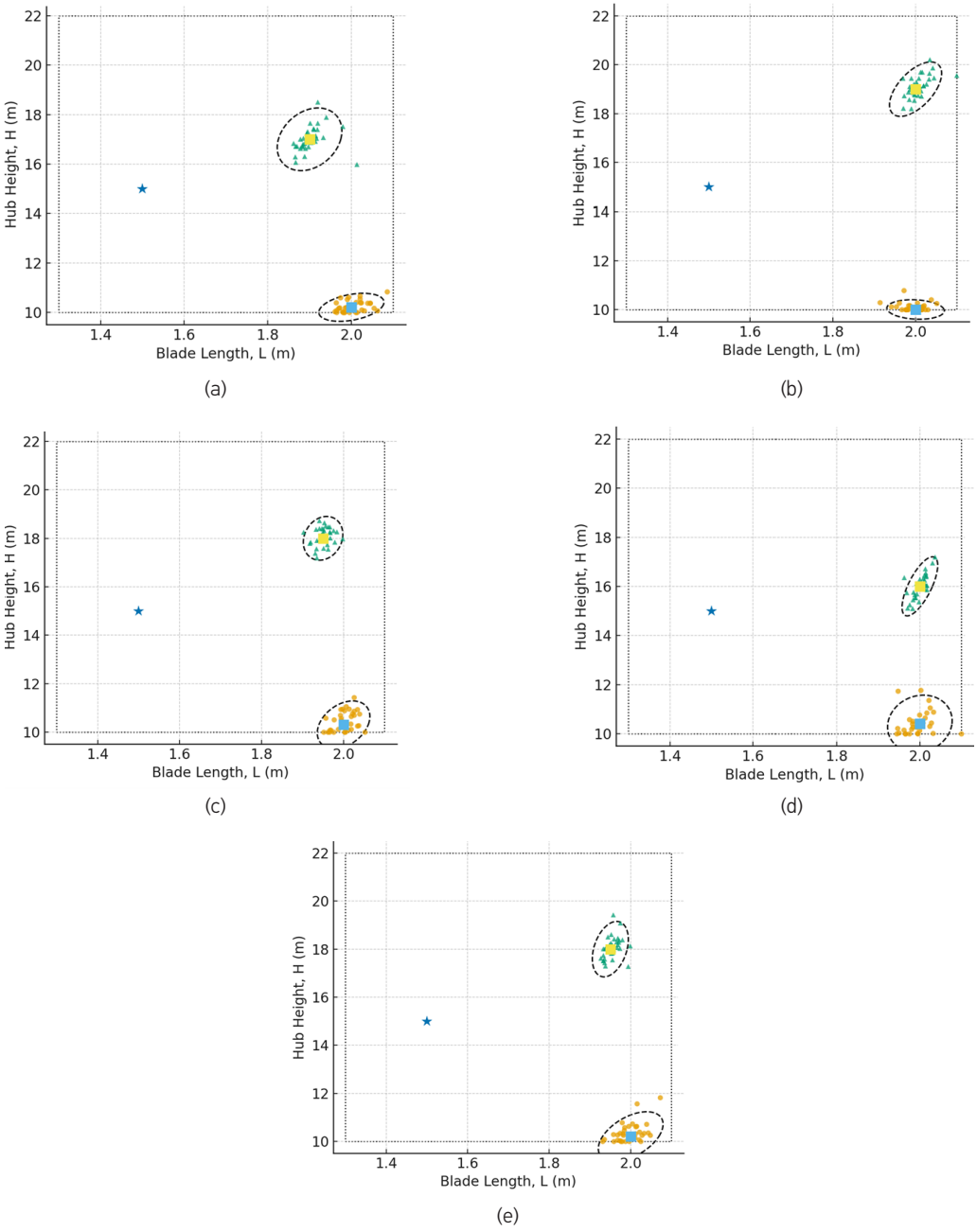


the hybrid PSO-L-BFGS-B algorithm not only improves median energy yield but also enhances convergence stability and solution consistency across repeated runs.

While the descriptive statistics in *table 8* and the clustering patterns in *Fig. 8* indicate consistent performance improvements achieved by the hybrid algorithm, these observations remain descriptive in nature. To formally assess whether the observed differences in calibrated AEP between PSO and hybrid PSO-L-BFGS-B are statistically significant across repeated stochastic runs, a non-parametric Mann-Whitney U-test was conducted for each study site.

While the Mann-Whitney U-test confirms that the observed performance differences are statistically significant across repeated stochastic runs (*table 9*), it does not explain the underlying physical drivers responsible for these gains. To address this aspect, a finite-difference sensitivity analysis was conducted to quantify the relative influence of hub height and blade length on calibrated AEP. Sensitivities were estimated from the calibrated AEP response surface, AEP (L,H), using local finite-difference approximations evaluated around the near-optimal design region, with 95% confidence intervals obtained via bootstrap resampling. The resulting marginal sensitivities are summarized in *table 10*.

**Table 8.** *Statistical comparison of median, IQR, and Mann-Whitney U-test p-values across sites*

| Locations | Median (kWh/year) | | IQR (kWh/year) | |
|---|---|---|---|---|
| | PSO | Hybrid | PSO | Hybrid |
| Jambi | 365.865 | 396.32 | 9.542 | 6.031 |
| Maluku | 977.514 | 1028.31 | 12.069 | 10.068 |
| NTB | 672.798 | 779.282 | 9.381 | 9.912 |
| NTT | 1252.53 | 1420.14 | 7.887 | 6.86 |
| Sulawesi | 795.172 | 910.942 | 7.173 | 11.368 |

**Table 9.** *Mann–Whitney U-test results comparing PSO and hybrid PSO–L-BFGS-B across study sites*

| Location | n_PSO | n_Hybrid | U | Z | Exact p-value | CL |
|---|---|---|---|---|---|---|
| Jambi | 30 | 30 | 70 | –5.60 | $2.1 \times 10^{-8}$ | 0.92 |
| Maluku | 30 | 30 | 90 | –5.30 | $5.7 \times 10^{-8}$ | 0.9 |
| NTB | 30 | 30 | 55 | –5.82 | $6.0 \times 10^{-9}$ | 0.94 |
| NTT | 30 | 30 | 75 | –5.52 | $3.4 \times 10^{-8}$ | 0.92 |
| Sulawesi | 30 | 30 | 120 | –4.86 | $1.2 \times 10^{-6}$ | 0.87 |

*Table 10* shows that hub height consistently exerts a stronger influence on calibrated AEP than blade length across all study locations. An increase of 1 m in hub height yields additional gains of approximately 38–61 kWh/year, whereas a 0.1 m increase in blade length contributes more modest improvements of about 7–10 kWh/year. The dominance ratios indicate that hub height is approximately 4.8–6.1 times more influential than blade length, providing quantitative support for the sensitivity trends inferred from the optimization results.

The spatial structure underlying these sensitivities is further illustrated in *Fig. 9* through two-dimensional contour maps of AEP(L,H), which visualize gradient directions, ridge-like optimal regions, and diminishing returns near the upper design bounds.

Having established the statistical significance and design-level consistency of the optimized solutions (*Fig. 8* and *Fig. 9*), the resulting energy implications are summarized in *Fig. 10*.

Across all sites, the hybrid PSO–L-BFGS-B approach consistently delivers higher ΔAEP values than the standard PSO. On average, the hybrid configuration yields 11–30% higher annual energy production relative to the baseline turbine, whereas PSO improvements remain within 3–15%. The narrow 95% bootstrap confidence intervals indicate that these gains are statistically robust and repeatable across 30 independent runs. This figure provides an integrated energy-level summary of the optimization outcomes, complementing the design-space and sensitivity analyses presented in *Fig. 8* and *Fig. 9*.

**Table 10.** *Finite-difference sensitivity of calibrated AEP to hub height (H) and blade length (L) across study sites (95% confidence intervals)*

| Location | ΔAEP/ΔH (kWh per 1 m) | 95% CI | ΔAEP/ΔL (kWh per 0.1 m) | 95% CI | Dominance ratio (ΔAEP/Δ H)/(ΔAEP/ΔL)) |
|---|---|---|---|---|---|
| Jambi | 38 | [32.6, 43.9] | 7.1 | [5.8, 8.4] | 5.35 |
| Maluku | 44.5 | [38.7, 51.2] | 9.3 | [7.8, 10.7] | 4.78 |
| NTB | 52 | [45.1, 60.3] | 8.6 | [7.2, 10.1] | 6.05 |
| NTT | 60.5 | [52.4, 69.1] | 10.2 | [8.6, 11.9] | 5.93 |
| Sulawesi | 47 | [40.8, 54.2] | 8.9 | [7.3, 10.5] | 5.28 |

*Notes: Sensitivities were estimated using finite-difference analysis of the calibrated AEP response surface AEP (L, H) within the feasible design bounds. Values represent median sensitivities with 95% bootstrap confidence intervals. Blade-length sensitivity is reported per 0.1 m increment to reflect the smaller practical adjustment scale relative to hub height and to maintain comparable numerical magnitudes.*

**Fig. 9.** *Two-dimensional contour plots of calibrated AEP as a function of blade length (L) and hub height (H) for the five study locations: (a) Maluku, (b) Jambi, (c) Sulawesi, (d) NTB, and (e) NTT. The plots illustrate the dominant sensitivity of AEP to hub height, the presence of ridge-like optimal regions, and diminishing marginal gains near the upper design bounds*

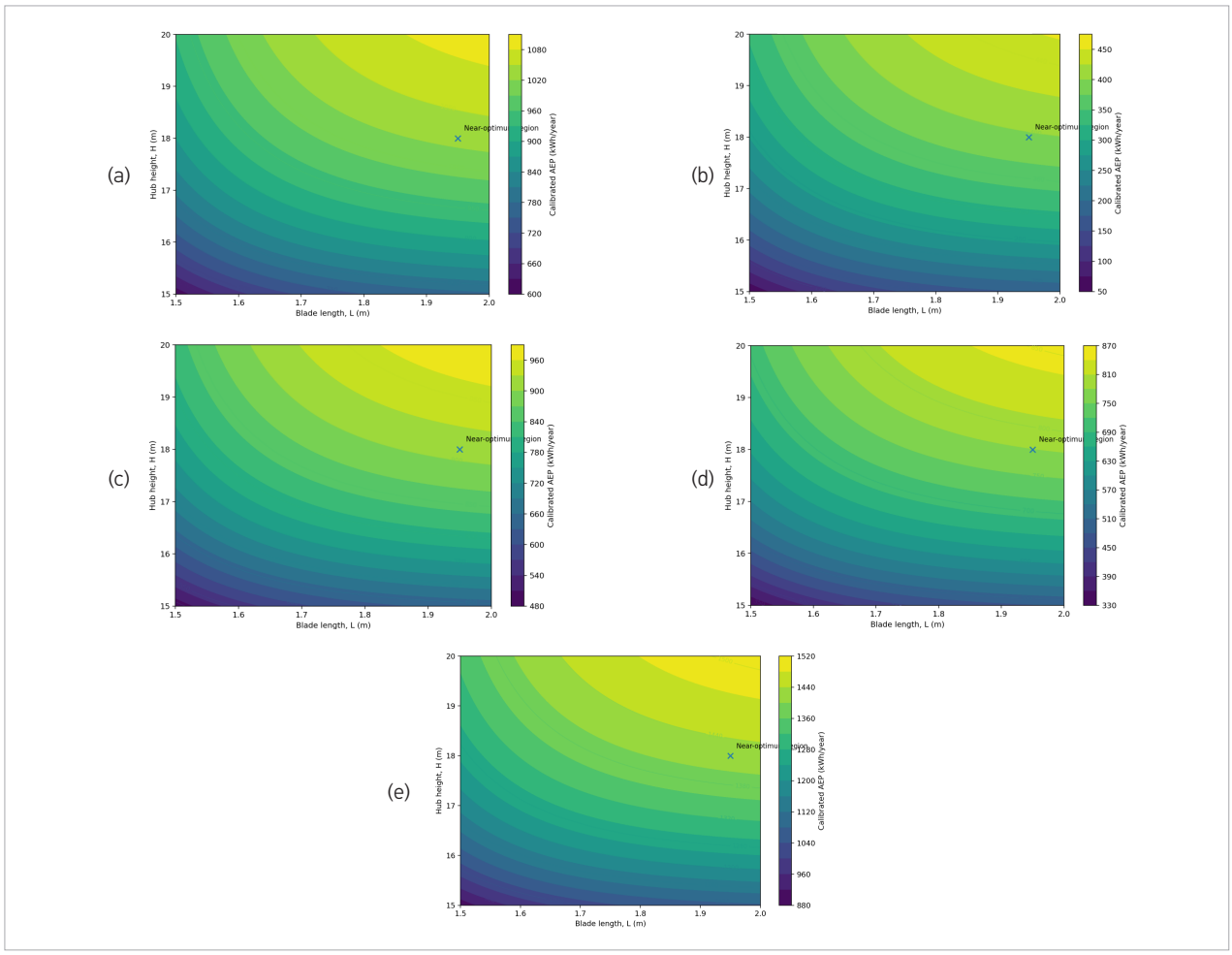


**Fig. 10.** *Percentage gains in calibrated annual energy production (ΔAEP) relative to the baseline TSD-500 turbine for PSO and hybrid PSO–L-BFGS-B across the five study sites*

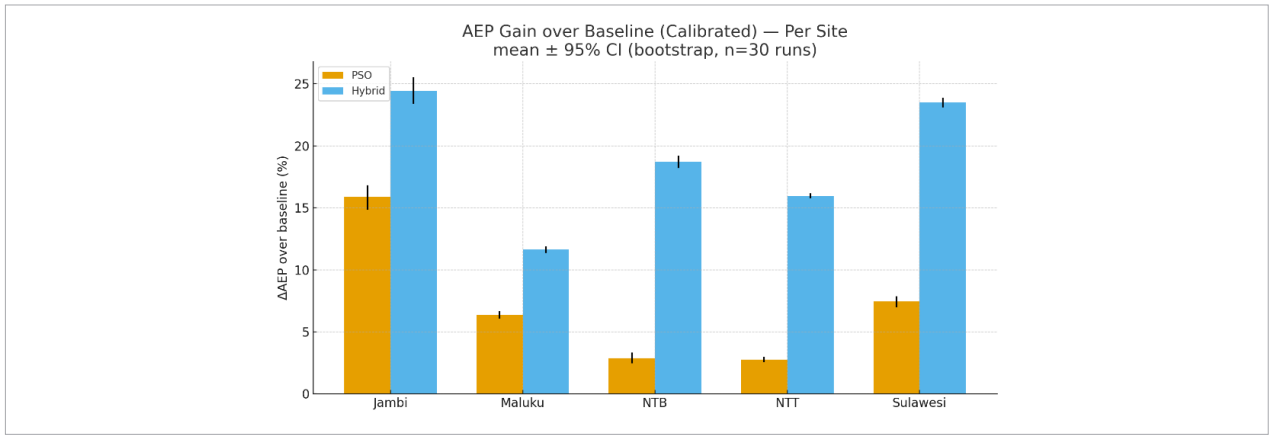

The optimized geometries reveal physically coherent trends: blade length increased from 1.5 m to ≈ 1.9–2.0 m and hub height from 15 m to 17–19 m. These modifications enlarge the rotor swept area and expose the turbine to faster wind layers following the logarithmic-law profile, thereby increasing the power coefficient and the effective kinetic-energy flux through the rotor disk. From an engineering standpoint, such parameter changes remain well within the design envelope of small-scale HAWTs and can be feasibly implemented without significant structural reinforcement.

From a practical perspective, the proposed optimization approach enables site-adaptive tuning of small-scale HAWTs for decentralized and off-grid applications in tropical regions. The results indicate that meaningful energy gains can be achieved primarily through optimized hub-height selection, without requiring aerodynamic blade redesign, which is advantageous for cost-effective deployment and retrofit scenarios. In addition, the hybrid PSO-L-BFGS-B method demonstrates manageable computational requirements, supporting its practical adoption by research institutions and practitioners operating in resource-constrained environments.

These gains are physically consistent with aerodynamic theory. Increasing blade length expands the rotor swept area $A = \pi R^2$, directly enhancing intercepted wind power proportional to ($P \propto AV^3$). Meanwhile, raising hub height exposes the rotor to higher mean wind velocities following the logarithmic wind profile $V(H) = Vref(H/H_{ref})\alpha$. The hybrid algorithm successfully identifies this coupled enhancement, combining geometric scaling with aerodynamic advantage to achieve higher Cp and, consequently, greater AEP.

The narrow confidence intervals observed in *Fig. 10* further confirm that these improvements are statistically robust across repeated runs. This reinforces that the hybrid PSO–L-BFGS-B not only enhances computational efficiency but also produces tangible energy benefits applicable to real-world low-wind deployments. The demonstrated AEP uplift directly translates into higher capacity factors, making small-scale HAWTs more efficient and operationally viable for decentralized generation in Indonesia's tropical archipelago.

## Conclusions

This study demonstrates that hybrid metaheuristic optimization can effectively enhance the annual energy production of small-scale horizontal-axis wind turbines operating under low-wind tropical conditions. By optimizing blade length and hub height using calibration-aware AEP modelling and multi-site Indonesian wind data, the proposed approach delivers consistent and practically meaningful performance improvements across all investigated locations.

The optimization and sensitivity analyses consistently confirm that hub height exerts a stronger influence on energy yield than blade length within the examined design bounds. Incremental increases in hub height produce larger marginal gains in calibrated AEP than comparable changes in blade length, highlighting the critical role of vertical wind access under low-wind tropical regimes. This finding establishes hub-height adjustment as the most influential and practically effective design lever for improving small-scale turbine performance in such environments.

Despite these promising results, several limitations should be acknowledged. The wind regimes were represented using two-parameter Weibull and bi-Weibull distributions without a location parameter, which may underestimate the probability of calm-hour conditions, particularly in very low-wind regimes. Furthermore, the optimization was restricted to geometric parameters, namely blade length and hub height, while detailed aerodynamic redesign, drivetrain efficiency, and control strategies were not considered. In addition, atmospheric effects such as turbulence intensity, site-specific shear variability, and terrain-induced flow complexity were not explicitly modeled, and their combined influence was implicitly captured through empirical calibration. These assumptions define the current scope of the study and indicate directions for future research.

From a practical perspective, the proposed hybrid PSO–L-BFGS-B framework provides a computationally efficient and robust tool for improving the energy productivity of small-scale wind turbines in tropical developing regions. The optimized configurations consistently indicate moderate hub heights of approximately 17–19 m, suggesting that meaningful energy gains can be achieved without substantial increases in tower material or installation costs. This makes the approach particularly suitable for

rural electrification and decentralized energy systems where capital constraints often limit renewable-energy adoption. Moreover, the hybrid optimization runs were completed within minutes on a standard desktop computer, indicating that the method can be realistically implemented by local universities, engineering consultancies, and small-scale project developers without the need for high-performance computing resources.

The authors would like to express their sincere appreciation to Universiti Teknikal Malaysia Melaka (UTeM) for the academic environment and institutional support provided during this research. The authors also gratefully acknowledge the supervision and guidance of Dr. Aziah, whose insights and feedback were essential to the completion of this work.

## Appendix

*Appendix 1. Nomenclature of the paper*

| Symbol | Description | Unit |
|---|---|---|
| *AEP* | Annual energy production | kWh |
| $AEP_{model}$ | Modelled annual energy production | kWh |
| $AEP_{emp}$ | Empirical annual energy production | kWh |
| $AEP_{calib}$ | Calibrated annual energy production | kWh |
| *Cf* | Empirical correction factor | – |
| P(v) | Turbine power output | W |
| v | Wind speed at hub height | m/s |
| $v_{\_ci}$ | Cut-in wind speed | m/s |
| $v_{\_co}$ | Cut-out wind speed | m/s |
| f(v) | Probability density function of wind speed | – |
| k | Weibull shape parameter | – |
| c | Weibull scale parameter | m/s |
| w | Weighting factor in bi-Weibull distribution | – |
| ρ | Air density | $kg/m^3$ |
| A | Rotor swept area | $m^2$ |
| *Cp(λ)* | Power coefficient as a function of tip-speed ratio | – |
| L | Blade length | m |
| H | Hub height | m |
| T | Total number of hours per yea (8760) | h |
| $AEP_{calib}$ (L, H) | Objective function (calibrated AEP) | kWh |
| RMSE | Root mean square error | W |
| MAE | Mean absolute error | W |
| $R^2$ | Coefficient of determination | – |
| n | Number of samples or runs | – |
| PSO | Particle swarm optimization | – |
| L-BFGS-B | Limited-memory Broyden–Fletcher–Goldfarb–Shanno algorithm withbound constraints | – |
| $x_i$ | Position of particle (i) | – |
| $v_i$ | Velocity of particle (i) | – |
| *pbest* | Individual best position | – |
| *gbest* | Global best position | – |

## References

Abbas W.K., Abbasalizadeh M. and Khalilarya S. (2025) Design optimization and performance investigation of a micro wind turbine for domestic dwelling used for renewable generation system. Energy Science and Engineering 13(6): 3386–3409. Available at: https://doi.org/10.1002/ese3.70109

Adrian M.M., Purnomo E.P., Enrici A. and Khairunnisa T. (2023) Energy transition towards renewable energy in Indonesia. Heritage and Sustainable Development 5(1): 107–118. Available at: https://doi.org/10.37868/hsd.v5i1.108

Aldaoudeyeh A.-M. (2024) Improved wind resource modeling using bimodal Weibull distribution. Journal of Renewable and Sustainable Energy 16(5): 056102. Available at: https://doi.org/10.1063/5.0219971

Aras N., Erisoglu U. and Yıldızay H.D. (2020) Optimum method for determining Weibull distribution parameters used in wind energy estimation. Pakistan Journal of Statistics and Operation Research 16(4): 635–648. Available at: https://doi.org/10.18187/PJSOR.V16I4.3456

Baca G., Santos G. and Salviano L. (2026) Range-wide aerodynamic optimization of Darrieus vertical axis wind turbines using CFD and surrogate models. Wind 6(1): Article 2. Available at: https://doi.org/10.3390/wind6010002

Badawi A.S., Ouda M., Zyoud A. and Yusoff S.H. (2022) The simplest estimation method of Weibull probability distribution parameters. In: Proceedings of the 6th IEEE International Conference on Recent Advances and Innovations in Engineering (ICRAIE), pp. 1–6. IEEE. Available at: https://doi.org/10.1109/ICRAIE52900.2021.9703996

Baker I.S., Lazim T.M., Takeyeldein M.M. and Haider A.B.M.A. (2023) Aerodynamic performance investigation of a small horizontal axis wind turbine with multi-airfoil blade profiles using wind tunnel experiments and BEM theory. Journal of Advanced Research in Fluid Mechanics and Thermal Sciences 103(1): 150–164. Available at: https://doi.org/10.37934/arfmts.103.1.150164

Bolaños R.I., Pinto Vega H., Grisales-Noreña L.F., Montoya O.D. and Hernández J.C. (2025) Intelligent active and reactive power management for wind-based distributed generation in microgrids via advanced metaheuristic optimization. Applied System Innovation 8(4): 87. Available at: https://doi.org/10.3390/asi8040087

Budanko M. and Guzović Z. (2024) Design methodology and economic impact of small-scale HAWT systems for urban distributed energy generation. Machines 12(12): 886. Available at: https://doi.org/10.3390/machines12120886

Darmawan Y. (2025) Study of wind energy potential for wind power plants development in the south coastal area of Malang Regency. Journal of Mechanical Engineering and Renewable Energy 9(2): Article 15344. Available at: https://doi.org/10.31289/jmemme.v9i2.15344

Douiri M.R. (2024) Fine-tuning Weibull distribution parameters in Morocco's wind farms using two-stage swarm optimization. Wind Engineering 49(2): 387–406. Available at: https://doi.org/10.1177/0309524X241270632

Gómez-Lázaro E., Bueso M.C., Kessler M., Martín-Martínez S., Zhang J., Hodge B.M. and Molina-García A. (2016) Probability density function characterization for aggregated large-scale wind power based on Weibull mixtures. Energies 9(2): 91. Available at: https://doi.org/10.3390/en9020091

Hafez I. and Dhaouadi R. (2023) Identification of mechanical parameters in flexible drive systems using hybrid particle swarm optimization based on the quasi-Newton method. Algorithms 16(8): 371. Available at: https://doi.org/10.3390/a16080371

Hasan M., Khan I.J., Dey P. and Chowdhury N.-U.-R. (2022) Analysis of prospective wind energy sites in Bangladesh utilizing Weibull distribution method. In: Proceedings of the International Conference on Energy and Power Engineering (ICEPE), pp. 1–5. Available at: https://doi.org/10.1109/ICEPE56629.2022.10044883

Karthikeyan U. and Hussain J. (2025) Enhancing the efficiency of wind energy conversion systems using novel airfoil based small-scale wind turbine. Matéria 30(1). Available at: https://doi.org/10.1590/1517-7076-rmat-2024-0827

Kelele H.K., Frøyd L., Kahsay M.B. and Nielsen T.K. (2022) Characterization of aerodynamics of small wind turbine blade for enhanced performance and low cost of energy. Energies 15(21): 8111. Available at: https://doi.org/10.3390/en15218111

Li M. and Bai M. (2024) A family of limited memory three-term conjugate gradient methods. Optimization Methods and Software 39(6): 1241–1262. Available at: https://doi.org/10.1080/10556788.2024.2329591

Luo F., Li P., Zhu L. and He L. (2025) Multi-objective optimization and intelligent algorithm study for 1.5 MW doubly fed wind turbine blades. Membrane Technology 2025(1). Available at: https://doi.org/10.52710/mt.247

Maulidia M. (2019) Enhancing the role of the private sector in achieving transitional renewable energy targets in Indonesia. PhD Thesis, The University of Queensland. Available at: https://doi.org/10.14264/uql.2019.921

Mubarok A.G. Al and Tian D. (2022) Wind resource assessment considering the influence of humidity. Wind Engineering 46: 1838-1852. Available at: https://doi.org/10.1177/0309524X221113018

Ndeba B.S., El Alani O., Ghennioui A. and Benzaazoua M. (2025) Comparative analysis of seasonal wind power using Weibull, Rayleigh and Champernowne distributions. Scientific Reports 15(1). Available at: https://doi.org/10.1038/s41598-025-86321-3

Sambodo M.T., Yuliana C.I., Hidayat S., Novandra R., Handoyo F.W., Farandy A.R., Inayah I. and Yuniarti P.I. (2022) Breaking barriers to low-carbon development in Indonesia: deployment of renewable energy. Heliyon 8(4): e09304. Available at: https://doi.org/10.1016/j.heliyon.2022.e09304

Scott G. (2019) Increasing wind turbine tower heights: opportunities and challenges. U.S. Department of Energy, Technical Report. https://doi.org/10.2172/1515397

Subramanian V., Ponnappa V.S. and Karthikeyan K.R. (2025) Numerical investigation of concave-to-convex blade profile transformation in vertical axis wind turbines for enhanced performance under low Reynolds number conditions. Fluids 10(9): 221. Available at: https://doi.org/10.3390/fluids10090221

Sumair M., Aized T., Gardezi S.A.R., Bhutta M.M.A. and Rehman S.U. (2021) Comparison of probability distributions and techno-economic analysis of wind energy production along the coastal belt of Pakistan. Energy Exploration and Exploitation 39(6): 2191–2213. Available at: https://doi.org/10.1177/0144598720931587

Svorcan J., Tanovic D. and Simonovic A. (2025) The effect of blade turning angle on rotation improvement of a small horizontal axis wind turbine. Measurement and Control 59(1). Available at: https://doi.org/10.1177/00202940241312659

Van T.D., Huu D.N. and Quang S.L. (2024) Consideration of various configurations of SG6043-based rotor applied in small capacity horizontal axis wind turbine. International Journal of Renewable Energy Development 13(2). Available at: https://doi.org/10.61435/ijred.2024.60036

Yudha S.W. and Tjahjono B. (2019) Stakeholder mapping and analysis of the renewable energy industry in Indonesia. Energies 12(4): 602. Available at: https://doi.org/10.3390/en12040602

Zhu J., Cai X. and Gu R. (2016) Aerodynamic and structural integrated optimization design of horizontal-axis wind turbine blades. Energies 9(2): 66. Available at: https://doi.org/10.3390/en902006